


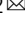

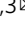



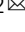



Andean-type orogenic plateau as a trigger for aridification in the arcs of northeast Pangaea

Dongfang Song ^{1,2}, Ross N. Mitchell ^{1,2}, Wenjiao Xiao ^{1,2,3}, Qigui Mao ³, Bo Wan ^{1,2} & Songjian Ao ^{1,2}

The interplay between continental motions during the assembly of Pangaea and late Palaeozoic climate change, including severe glaciation and global aridification, remains enigmatic. Here we identify the provenance of Permian–Early Triassic sediments that recorded climate change of North China and estimate palaeoelevation to constrain tectonic–climate interaction during the assembly of northeast Pangaea. Detrital zircon U–Pb–Hf analysis indicates the sediments were locally sourced from the ancient basement and associated with a late Palaeozoic (410–260 million years ago) continental arc, devoid of input from juvenile arcs of the Altaiids. These sediments were interpreted as deposited in a retroarc foreland basin ascribed to subduction of the Palaeo-Asian Ocean. Crustal thickness estimated from whole-rock La/Yb yields an average value of 58 ± 11 km, which corresponds to a palaeoelevation of 3.8 ± 0.7 km. The results reveal the existence in North China of an orogenic plateau comparable to the Altiplano of the Andes that blocked moisture transport from the ocean and served as an important orographic barrier to trigger Permian aridification.

¹State Key Laboratory of Lithospheric Evolution, Institute of Geology and Geophysics, Chinese Academy of Sciences, Beijing 100029, China.

²Innovation Academy for Earth Science, Chinese Academy of Sciences, Beijing 100029, China. ³National Key Laboratory of Ecological Safety and Sustainable Development in Arid Lands, Xinjiang Institute of Ecology and Geography, Chinese Academy of Sciences, Urumqi 830011, China.

email: dfsong@mail.iggcas.ac.cn; ross.mitchell@mail.iggcas.ac.cn; wj-xiao@mail.iggcas.ac.cn; asj@mail.iggcas.ac.cn

While the Andes serve as a neotectonic exemplar of continental arc magmatism and flat-slab (ridge/seamount-induced) subduction that has been useful to understand the geologic past^{1,2}, another potential Andean neotectonic aspect—orographic-precipitation-induced aridification as has occurred in the Atacama desert—remains underexplored in Earth's past. The initiation and termination of the late Palaeozoic ice age (340–250 Ma) is one of the most prominent climate change events in Earth history and coincided with the assembly of supercontinent Pangaea and global aridification³. Although the fall and rise of atmospheric CO₂ has been considered as a leading factor controlling this severe climate change⁴, recent studies suggest that the uplift of the equatorial Hercynian Mountains and the assembly of Pangaea had potential effects on the tumultuous late Palaeozoic climate change⁵.

Accompanying Hercynian orogenesis in the core of Pangaea, the long-lived subduction of the Palaeo-Asian Ocean (PAO) gave birth to the world's largest Palaeozoic accretionary orogen, the Central Asian Orogenic Belt (CAOB; a.k.a. the Altaids) in northeast Pangaea^{6,7}, which is currently situated between the Baltica and Siberia cratons to the north and the Tarim and North China cratons to the south (Fig. 1a). The Xing'an–Inner Mongolia Orogen in the southeastern segment of the CAOB (Fig. 1a, b) was formed through the complex amalgamation between the South Mongolia arc-accretionary complex and the North China craton after the final closure of the PAO^{8,9}.

One major manifestation of severe climate change during the assembly of northeast Pangaea was the Permian aridification of North China craton¹⁰ (hereafter referred to as simply North China). The aridification coincided with the largest extinction of biodiversity, of both regional-scale genera and species, ever documented in North China¹¹. The orogenic processes of the CAOB potentially promoted this climate change as North China was the southern shoreline margin of the subducting PAO during the late Palaeozoic^{12,13}. However, the timing of the closure of the PAO and the orogenic architecture of the southern CAOB during

the Permian remains highly controversial^{14–16}. Moreover, no quantification of late Palaeozoic surface topography has been obtained to date for the northern margin of North China. These ambiguities in temporal and spatial evolution of orogeny have led to much uncertainty in the palaeogeographic and palaeotopographic reconstruction of northeast Pangaea and the potential feedbacks between orogenic dynamics and climate change. The role of the tectonic boundary conditions in the Permian climatic evolution of North China remains unclear.

Sedimentary basins formed during orogenesis are the earliest and most sensitive archives that record orogenic processes and growth and erosion of topography¹⁷. Permian–Triassic sedimentary successions intermittently distributed along the northern margin of North China contain critical information of temporal and spatial variations in magmatic activity, exhumation and palaeoclimate change, and provide excellent recorders for tracing tectonic–climatic feedbacks of the adjacent convergent margin during the assembly of northeast Pangaea.

Here we present an integrated sedimentological and geochronologic study of Permian–Early Triassic sediments in northern North China to evaluate the provenance, basin development and tectonic setting. In addition, we compiled whole-rock La/Yb data for late Carboniferous to Permian magmatic rocks to estimate the crustal thickness and palaeoelevation of the northern margin of North China. The results indicate the development of a Permian–Early Triassic retroarc foreland system with an Andean-type orogenic plateau in northern North China, which revises the current understanding of the late Palaeozoic tectonic evolution of the southeastern CAOB and the mechanism of Permian aridification in North China.

Results

Stratigraphy and sedimentology. Permian to Early Triassic sedimentary rocks crop out in the Daqingshan area of North China. They unconformably overlie Ordovician carbonates or are in fault contact with the Proterozoic metamorphic basement (gneiss-schist

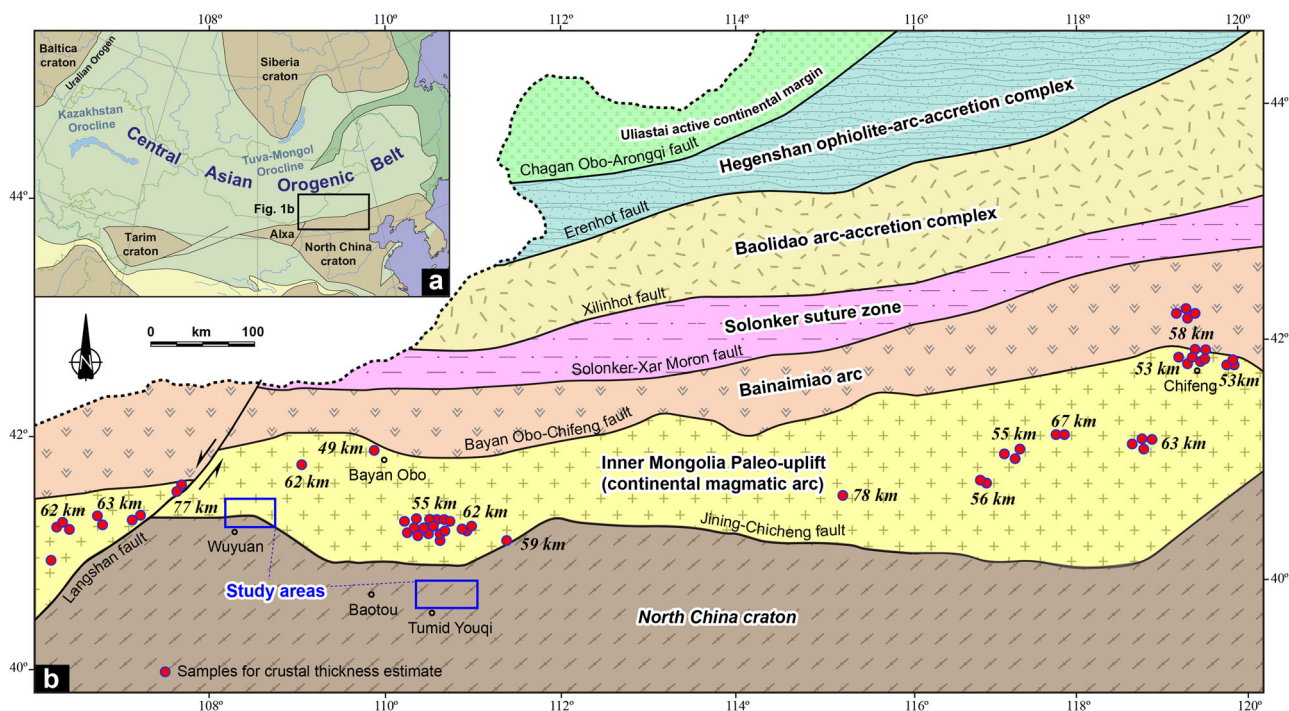


Fig. 1 Tectonic map of the study area. **a** Regional tectonic map of the Central Asian Orogenic Belt showing the location of the study area (modified with permission from ref. ⁸⁷, Elsevier). **b** Tectonic map of Inner Mongolia showing the major lithologic–tectonic units discussed in this study (modified with permission from ref. ⁹, Wiley).

complexes) of North China. We studied in detail the Wuyuan and Tumid sections where a continuous Permian to Early Triassic stratigraphy is well exposed (Supplementary Fig. 1a, b). Permian sedimentary rocks in the Dahongshan area, ~30 km north of Wuyuan county, are mapped as the Dahongshan Formation¹⁸, which rests unconformably on or is in fault contact with Mesoproterozoic metamorphic rocks of the Zhaertai Group, and are intruded by Permian granitoids (Supplementary Fig. 1a).

The Dahongshan Formation has a total thickness of ~5000 m and consists of coal-bearing clastic rocks and volcanoclastic rocks in the lower and upper part, respectively¹⁸. It is subdivided into five rock members based on lithologic characteristics. The basal member (P_1d^1) consists of black thick-bedded conglomerate with interbedded pebbly sandstone, carbonaceous slate and limestone lens. The second member (P_1d^2) contains carbonaceous slate, tuff and pebbly sandstone, with local occurrences of 1–2-m thick coal seams (Supplementary Fig. 2a, b). Rhythmic structures are well developed in the tuff (Supplementary Fig. 2c). The widely-distributed third member (P_1d^3) mainly consists of conglomerate, sandstone, carbonaceous slate and tuff (Supplementary Fig. 2d–f). The conglomerates are thickly bedded with thickness reaching up to 150 m. They are sandy-matrix-supported and include moderately sorted, fine- to medium-grained (1–6 cm), subrounded pebbles dominated by quartzite and granitoid, with subordinate mudstone, tuff and metamorphic rocks. Several coal seams are present within the sandstone and slate. The fourth member (P_1d^4) contains primarily black conglomerate interbedded with grey feldspar quartz sandstone (Supplementary Fig. 2g, h) and minor marlstone (Supplementary Fig. 2i). Parallel and trough/planar cross beddings are preserved in the sandstone. The fifth member (P_1d^5) mainly consists of tuffaceous sandstone, tuff, carbonaceous slate and andesitic porphyrite. The lithofacies associations, including sandy-matrix-supported conglomerate, trough or planar cross-laminated sandstone, carbonaceous slate, marlstone and the development of coal seams, suggest that the Dahongshan Formation was deposited in the braided river delta plain.

Permian to Early Triassic sedimentary strata are well exposed ~10 km north of Tumid Youqi, Inner Mongolia (Supplementary Fig. 1b). These sediments rest unconformably on Cambrian–Ordovician shallow marine quartz sandstone and limestone, or are in fault contact with Archaean–Palaeoproterozoic metamorphic basement, and are unconformably overlain by Jurassic fluvial-lacustrine sediments. They have a total thickness of ~2000 m, and are folded into a major paired syncline–anticline. The Permian strata are divided into four formations (from bottom to top): the early Permian Shuanmazhuang Formation, the middle Permian Zahaigou Formation and Shiyewan Formation and the late Permian Naobaogou Formation.

The early Permian Shuanmazhuang Formation (P_1s) is the earliest nonmarine sedimentation resting unconformably on the Early Ordovician neritic facies sequence of the early Palaeozoic passive margin of North China. It mainly consists of grey conglomerate, pebbly sandstone and black-grey mudstone with the presence of coal seams reaching thicknesses of up to ~30 m (Supplementary Fig. 3a, b). The Shuanmazhuang Formation is folded into an anticline, and the duplex structure indicates northward thrusting (Supplementary Fig. 3b, c). Plant macrofossils of *Neuropteris pseudovata* and *Lepidodendron szeianum* were reported from this formation¹⁸. The field relationship and lithostratigraphy for the Permian strata that record information of climate change are summarised in Fig. 2. Contrasting lithologies and sedimentary facies occurred before and after the deposition of a thick-bedded conglomerate (Fig. 2a). The middle Permian Zahaigou Formation (P_2z) is composed of

grey-white conglomerate, sandstone, argillaceous rock and coal seams (Fig. 2b). The middle Permian Shiyewan Formation (P_2sy) contains thick-bedded conglomerate (Fig. 2c) with interbedded sandstone, siltstone and mudstone. The top of the Shiyewan Formation is conformably overlain by the red sandstone of the late Permian Naobaogou Formation (P_3n) that has a thickness of ~1100 m (Supplementary Fig. 3d). The Naobaogou Formation mainly consists of thick-bedded grayish purple polymictic conglomerate, purple medium bedded coarse-grained lithic feldspar sandstone, arkose and red siltstone (Fig. 2d, e and Supplementary Fig. 3e–g) and stands out in marked contrast to the underlying coal-bearing strata. Trough and tabular cross-stratification is well preserved within the sandstone (Supplementary Fig. 3e). The broadly tabular sandstone beds pinch out or thicken along strike, representing channelised sandbodies. Abundant nodular calcareous horizons, marl lens and gypsum crystals are observed within the red mudstone and siltstone. The conglomerate consists of sandy-matrix supported, 1–10 cm sized, pebbles of granites, porphyritic volcanic rocks, sandstones, cherts, schists, gneisses and quartzites (Supplementary Fig. 3e). The occurrence of mesoscale asymmetric folds indicates southward thrusting (Supplementary Fig. 3g). The Early Triassic Laowopu Formation (T_1lw) rests conformably on the late Permian Naobaogou Formation (Supplementary Fig. 3h). It has a total thickness of >550 m and represents the core of the major syncline. This formation mainly consists of purple sandstone, pebbly sandstone and conglomerate. Large-scale tabular and trough cross-stratification with foreset heights of up to 60 cm is developed within the sandstones (Supplementary Fig. 3i).

The lithologies and field characteristics of the Permian to Lower Triassic strata show that they are all terrestrial deposits. The early–middle Permian sediments are dominated by multi-storey sheet sandstone and conglomerate units with abundant scour surfaces and interbedded coal seams, suggesting a braided fluvial deposit in a coastal plain environment¹⁹. The presence of coal and abundant plant fossils implies a humid palaeoclimate during their deposition. The late Permian strata have sedimentary features with fining upwards and channelised nature of large sandbodies, pervasive tabular and trough cross-stratification, and abundant fine-grained siltstone and silty mudstone, which collectively indicate meandering fluvial and overbank deposition in a floodplain environment²⁰. The development of large-scale trough and planar cross-stratification, abundant traction and scour structures, and lack of fine-grained material suggest that the Early Triassic Laowopu Formation was likely a braided fluvial delta deposit. The presence of strong red coloration, calcic palaeosols and gypsum deposits indicate that the late Permian and Early Triassic sedimentation developed in an arid climate under strong oxidising conditions (Fig. 2d, e and Supplementary Fig. 3e, g–i). A remarkable climate change therefore is reflected in the transition from the coal-bearing unit to the continental redbed unit¹⁵.

Sampling strategy. Several sandstone samples from both the Wuyuan and Tumid sections were collected for petrologic and detrital zircon U–Pb and Lu–Hf isotopic analyses to investigate the provenances and tectonic settings for the Permian to Lower Triassic sediments (Supplementary Fig. 1a, b). One granite and one tuff sample associated with the sedimentary sequence were also collected for zircon U–Pb dating and Lu–Hf isotopic studies. To reconstruct the orography accompanying the sedimentation, whole-rock geochemical data for latest Carboniferous–Permian igneous rocks were compiled to estimate the crustal thickness and palaeoelevation of the northern margin of North China.

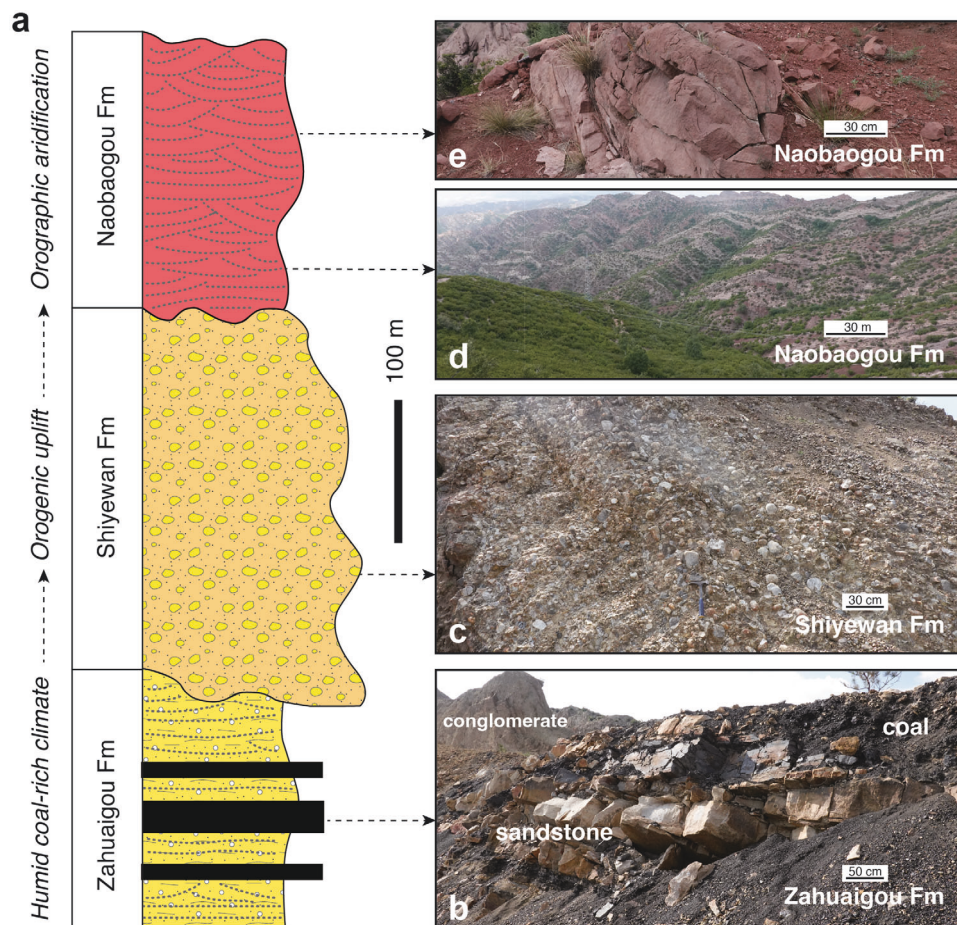


Fig. 2 Stratigraphy and field geology of the Permian sedimentary sequence. **a** Simplified lithostratigraphic column of the Tumid section showing thick-bedded conglomerate between the coal-bearing sandstone and continental redbeds, indicating the change from humid to arid climatic conditions occurred after a major tectonic uplift event. **b** Sandstone with interlayered coal seams indicating a humid climate. **c** Thick-bedded conglomerate. **d** Continental redbeds indicating an arid climate. **e** Close-up of red sandstone.

Petrography. The tuff from the Dahongshan Formation consists mainly of microcrystalline quartz (Supplementary Fig. 4a), and the sandstones are composed of monocrystalline and polycrystalline quartz, plagioclase, potassium feldspar, and a variety of lithic fragments including schist, gneiss and granite (Supplementary Fig. 4b, c). Accessory minerals include biotite, hornblende, pyroxene, magnetite and zircon. The grains are mostly angular, suggesting they were eroded directly from the bedrock with a relatively short distance of transport before deposition. Sandstones from the Permian strata of the Tumid section show apparently similar petrographic characteristics being dominated by angular-shaped monocrystalline and polycrystalline quartz, plagioclase, potassium feldspar and lithic fragments. Lithic grain compositions include volcanic rocks, granitic rocks, schist and gneiss, with less siltstone and sandstone (Supplementary Fig. 4d, e). Accessory minerals include biotite, zircon, magnetite and pyroxene. Sandstones from the Early Triassic Laowopu Formation contain grain-supported angular monocrystalline and polycrystalline quartz, potassium feldspar, plagioclase and lithic fragments of volcanic and metamorphic rocks (Supplementary Fig. 4f).

Zircon U-Pb and Lu-Hf isotopes. The zircon U-Pb isotopic results of the 16 analysed samples are presented in Supplementary Data 1. The concordia plots for the two igneous samples and the histograms and kernel density estimation plots (KDE) for detrital zircons of each sedimentary samples are presented in Supplementary Fig. 5. Zircon Lu-Hf isotopic compositions are listed in

Supplementary Data 2. The granite (21DHS01) and tuff (21DHS02) samples from the Wuyuan section have well-defined concordant ages yielding weighted mean values of 287 ± 1 Ma ($n = 22$, MSWD = 0.47) and 290 ± 1 Ma ($n = 30$, MSWD = 1.9), respectively (Supplementary Fig. 5a, b). They have average zircon $\epsilon_{\text{Hf}(t)}$ values of -6.5 and -19.8 , respectively. One hundred spots were analysed for each sandstone sample and a total of 1,400 detrital zircon U-Pb analyses were obtained, of which 1379 analyses yielded concordant ages. All samples of the Dahongshan Formation from the Wuyuan section yield three groups of detrital zircon U-Pb ages: Neoproterozoic–early Palaeoproterozoic (2750–2200 Ma), late Palaeoproterozoic (2100–1600 Ma) and late Palaeozoic (400–270 Ma), although the relative proportions of these age populations vary from sample to sample (Supplementary Fig. 5c). For example, samples 21DHS03, 21DHS09 and 21DHS14 have relatively lower proportions of Palaeozoic age populations compared to samples 21DHS07, 21DHS08 and 21DHS16. When the ages of all the samples are combined, they yield three major age peaks at ~ 2515 , 1756 and 297 Ma (Fig. 3a). The eight sandstone samples from the Tumid section also display comparable Neoproterozoic–early Palaeoproterozoic (2715–2200 Ma), late Palaeoproterozoic (2100–1600 Ma) and late Palaeozoic (400–260 Ma) detrital zircon U-Pb age spectrum on the KDE plots (Supplementary Fig. 5d). They together yield three prominent age peaks at ~ 2513 , 1845 and 304 Ma (Fig. 3a). A total of 162 spots with late Palaeozoic ages were further analysed for their Lu-Hf isotopic compositions. All the analysed spots yielded

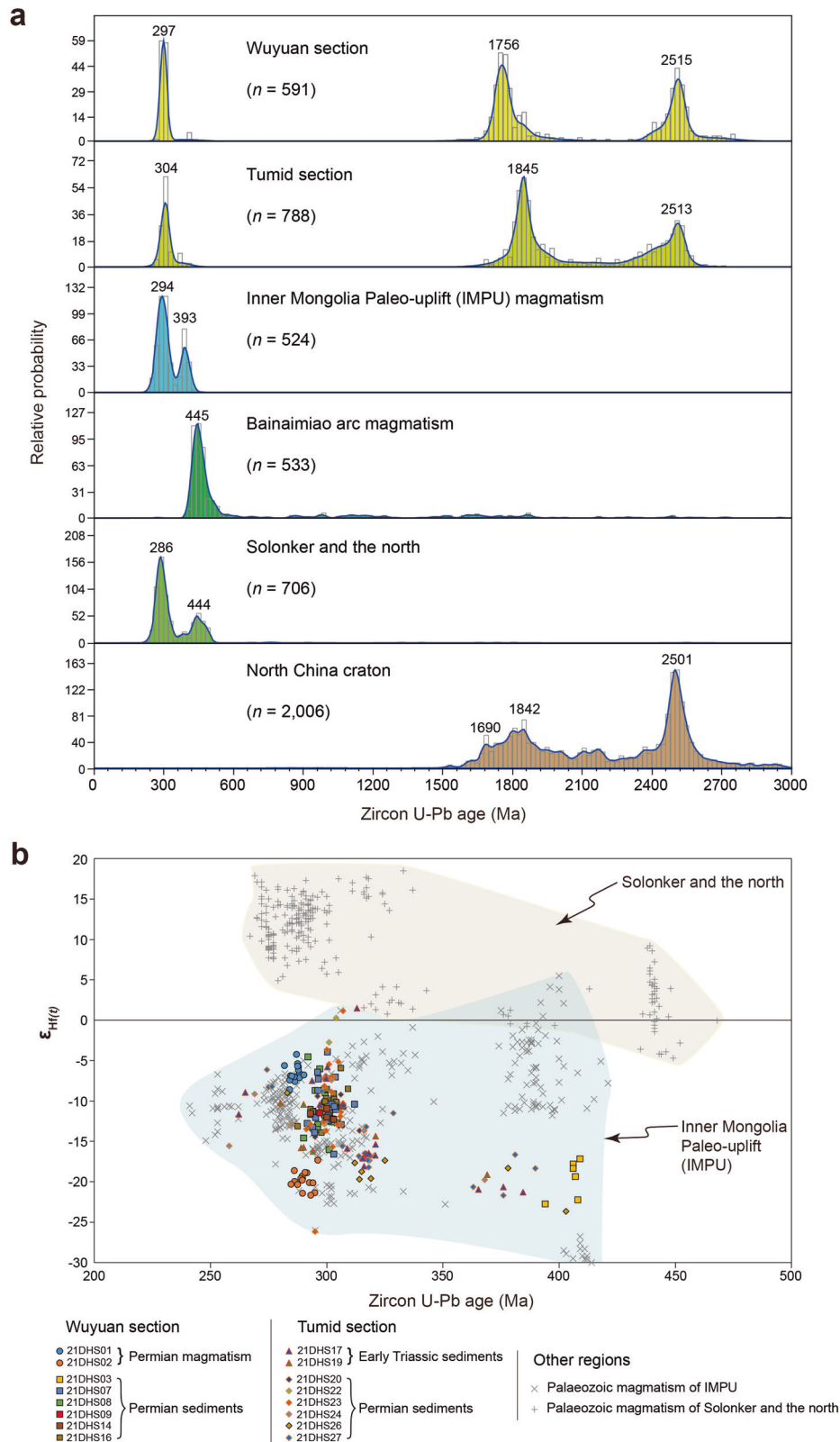


Fig. 3 Zircon U-Pb age distributions and zircon $\epsilon_{Hf(t)}$ values. **a** Comparison of age populations of the detrital zircons from this study and potential source regions. Blue lines are normalised kernel density estimation plots (KDE) and rectangles are age histograms. **b** Comparison between zircon $\epsilon_{Hf(t)}$ values of this study, Palaeozoic magmatism of the Solonker suture zone and regions to the north, and late Palaeozoic magmatism of the Inner Mongolia Palaeo-uplift (IMPU). Zircon U-Pb and Hf isotopic data for the Permian–Early Triassic samples are provided in Supplementary Data 1 and Supplementary Data 2, respectively. Compiled zircon U-Pb ages and $\epsilon_{Hf(t)}$ values from other regions for comparison are provided in Supplementary Data 3.

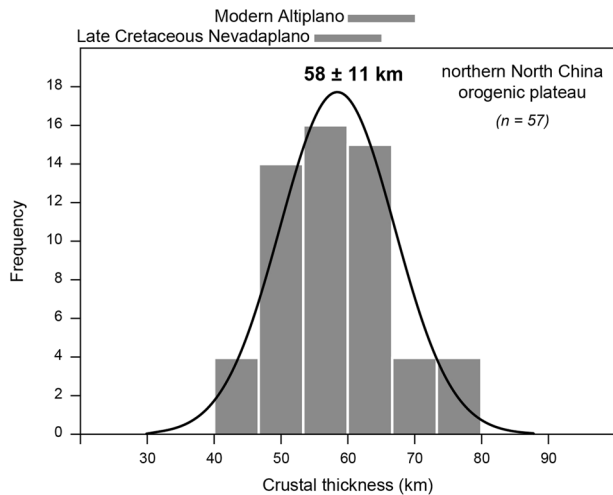


Fig. 4 Crustal thickness of the Permian orogenic plateau of northern North China. Histogram and Gaussian distribution depicting the average crustal thickness estimate (58 ± 11 km) for the Permian orogenic plateau of northern North China. The range of crustal thickness estimated for the Late Cretaceous Nevadaplano (55–65 km, North American Cordillera)⁴⁷ and for the modern Altiplano (60–70 km, Central Andes of the South American Cordillera)⁴⁹ are indicated for comparison. Crustal thickness, geochemical and location information for individual magmatic rocks are provided in Supplementary Data 4.

negative $\epsilon_{\text{Hf}(t)}$ values from -2.7 to -30.2 except for three analyses with slightly positive $\epsilon_{\text{Hf}(t)}$ values from 0.3 to 1.5 (Fig. 3b).

To determine the provenance of the sedimentary rocks, we compiled 3,769 zircon U–Pb ages and 565 Hf isotopic data from the potential source regions for comparison (Fig. 3a and Supplementary Data 3).

Crustal thickness. Estimates of crustal thickness using whole-rock La/Yb from individual rock analyses range from 41 to 78 km, with individual uncertainties from 9 to 13 km (Supplementary Data 4). Average crustal thickness estimates for areas with ≥ 3 samples (where available) are labelled in Fig. 1b to provide a representation of data variability. No clear correlation between age, location and calculated crustal thickness was distinguishable in the data set. Therefore, we suggest that the best estimate of crustal thickness during latest Carboniferous–Permian is obtained by considering the data collectively. The crustal thickness estimate results for the entire data set are plotted as a histogram (Fig. 4), which shows that most of the crustal thickness values distribute between 47 and 68 km. The 57 analyses yield a mean value of 58 ± 11 km (Fig. 4), which constrains the average crustal thickness of northern North China during the latest Carboniferous–Permian.

Discussion

Provenance analyses. The overall similar detrital zircon U–Pb age spectrum on the KDE plots for the samples from the Wuyuan and Tumid sections indicates that they have similar provenance signatures (Fig. 3a). The late Palaeozoic zircons are euhedral to subhedral with oscillatory zoning in cathodoluminescence (CL) images (Supplementary Fig. 6), implying they are of first-cycled magmatic origins. The presence of tuffs indicates an important sedimentary supply from a nearby active magmatic source. These are consistent with the petrographic characteristics of these sedimentary rocks that contain different proportions of volcanic fragments. Nearly all the late Palaeozoic zircons in both the Wuyuan and Tumid sections have negative $\epsilon_{\text{Hf}(t)}$ values (Fig. 3b),

indicating their derivation from late Palaeozoic magmatic rocks that formed from the reworking of substantial ancient continental crust. Widespread late Palaeozoic magmatic rocks exposed in the southern CAOB and the Inner Mongolia Palaeo-uplift (IMPU) are potential source regions for the late Palaeozoic detritus. Palaeozoic magmatic rocks from the various tectonic units of the southern CAOB, including the Bainaimiao arc, the Solonker suture zone, the Baolidao arc-accretion complex, and the Hegenshan ophiolite-arc-accretion complex exhibit mainly juvenile crustal signatures of intraoceanic subduction origins with little input from continental fragments⁷.

The Bainaimiao arc is characterised by magmatic and metamorphic rocks with zircon U–Pb ages between 520–410 Ma, dominated by a Late Ordovician–early Silurian (~ 445 Ma) peak^{21,22}, and Precambrian detrital zircon ages from Archaean to Neoproterozoic²³ (Fig. 3a). However, both early Palaeozoic and Mesoproterozoic–Neoproterozoic age populations are absent in the samples from the Wuyuan and Tumid sections (Fig. 3a). We therefore exclude the Bainaimiao arc as the source region for the Permian–Early Triassic sediments in this study. The Solonker suture zone is mainly composed of ophiolitic mélange, island arc tholeiite, mid-ocean-ridge basalt, tonalite and sanukitoid, with high $\epsilon_{\text{Nd}(t)}$ values from -0.7 to 8.4 and zircon $\epsilon_{\text{Hf}(t)}$ values from 14.7 to 19.1 , which together record the evolution of a Permian (~ 299 – 260 Ma) intraoceanic arc-trench system within the PAO^{24,25}. The Baolidao arc-accretion complex contains ~ 484 – 469 Ma Early Ordovician juvenile arc rocks with $\epsilon_{\text{Nd}(t)}$ values from 1.5 to 5.3 and initial $^{87}\text{Sr}/^{86}\text{Sr}$ ratios from 0.7043 to 0.7066 (ref. 26). Amphibolites from the Xilingol complex yield zircon U–Pb ages of 382 – 327 Ma with $\epsilon_{\text{Hf}(t)}$ values between -1.0 and 4.1 (ref. 27). Further north, the Hegenshan ophiolite arc-accretion complex contains late Palaeozoic ophiolitic mélanges and volcanic-plutonic complexes. Various Permian intrusions including adakites, alkaline granites, and A-type granites with zircon U–Pb ages of ~ 292 – 275 Ma and $\epsilon_{\text{Hf}(t)}$ from 4.9 to 20.3 have been reported in the Erenhot–Hegenshan belt of the central-northern Inner Mongolia^{28–30}. Therefore, the late Palaeozoic rocks from the southern CAOB have mainly positive zircon $\epsilon_{\text{Hf}(t)}$ values, which are different from the late Palaeozoic detrital zircons in the Permian–Early Triassic sediments with mainly negative $\epsilon_{\text{Hf}(t)}$ values (Fig. 3b). Thus, the various terranes north of the Bayan Obo–Chifeng fault also deemed as unlikely to have provided sedimentary sources for the Permian–Early Triassic strata in northern North China.

In contrast, the IMPU contains large-scale, late Palaeozoic magmatic rocks with negative whole-rock $\epsilon_{\text{Nd}(t)}$ and zircon $\epsilon_{\text{Hf}(t)}$ values. For example, granitoids with U–Pb ages of 324 – 274 Ma, $\epsilon_{\text{Nd}(t)}$ of -17.4 to -9.3 and $\epsilon_{\text{Hf}(t)}$ of -16.5 to 1.2 were reported from the eastern segment of the IMPU^{31,32}. Late Carboniferous–early Permian mafic-ultramafic complexes are characterised by low initial $^{87}\text{Sr}/^{86}\text{Sr}$ ratios of 0.70521 – 0.70604 , negative $\epsilon_{\text{Nd}(t)}$ values from -14.1 to -9.3 , and negative zircon $\epsilon_{\text{Hf}(t)}$ values from -17.0 to -10.5 , and were probably derived from metasomatized lithospheric mantle³³. In the western IMPU, early Permian (286 – 279 Ma) mafic to felsic intrusions with $\epsilon_{\text{Nd}(t)}$ of -13.9 to -4.67 and zircon $\epsilon_{\text{Hf}(t)}$ from -11.5 to -6.7 were reported in the Guyang area, north of Baotou³⁴. Early Permian (291 Ma) granitic plutons with low $\epsilon_{\text{Nd}(t)}$ (-15.1) and high initial $^{87}\text{Sr}/^{86}\text{Sr}$ (0.7073) were reported in the Wulatezhongqi region north of Wuyuan³⁵. In addition, along the Jining–Chicheng fault minor Devonian magmatism was reported, including an Early Devonian alkaline intrusive complex (whole-rock $\epsilon_{\text{Nd}(t)}$ values of -12.7 to -17.9 and zircon $\epsilon_{\text{Hf}(t)}$ values from -27.8 to -32.3 ; ref. 36), a Middle Devonian mafic complex³³, and A-type granites (~ 387 Ma; $\epsilon_{\text{Hf}(t)} = -11.5$ to -8.4 ; $T_{\text{DM}2} = 2820$ – 2548 Ma; ref. 37).

The $\epsilon_{\text{Hf}(t)}$ values of the Palaeozoic zircons from the Permian–Early Triassic sedimentary successions are within the range defined by the Palaeozoic magmatism of the IMPU, but are distinct from those of the Solonker suture zone and the regions north of it (Fig. 3b). Therefore, both the age spectrum and $\epsilon_{\text{Hf}(t)}$ values of the late Palaeozoic detrital zircons match well with those of the Palaeozoic magmatic rocks within the IMPU (Fig. 3a, b). Based on this synthesis, we suggest that the late Palaeozoic magmatic rocks within the IMPU were the sources for the late Palaeozoic detrital zircons in the Permian–Early Triassic sediments of this study.

The Neoproterozoic–Palaeoproterozoic age populations of the sampled strata, with major peaks at ~2515 Ma and ~1845–1756 Ma, are comparable to age peaks of the Precambrian basement of North China (Fig. 3a), which generally yield zircon U–Pb ages between 3600 and 1600 Ma, with major peaks at 2800–2400 and 2100–1700 Ma (ref. 38). Archaean (2571–2441 Ma) TTG (tonalite–trondhjemite–granodiorite) gneisses and Palaeoproterozoic (1962–1812 Ma) metasedimentary rocks were reported in the Daqingshan area of the IMPU¹⁵. Voluminous Neoproterozoic magmatic and metamorphic rocks dated at 2594–2502 Ma have been reported in the Guyang area in the western IMPU^{39,40}. Although the Alxa Block also contains Neoproterozoic–Palaeoproterozoic magmatic–metamorphic basement, the typical Mesoproterozoic–Neoproterozoic (1500–800 Ma) age signatures⁴¹ of the Alxa Block were not detected in this study, thus, we rule out the Alxa Block as a source region for the Permian–Early Triassic sediments. The Mesoproterozoic–Neoproterozoic age gap also excludes the southern Mongolian and Bainaimiao arcs as source regions as both of them contain numerous ages between 1200–750 Ma (refs. 23,38). The Neoproterozoic–Palaeoproterozoic zircons for the Permian–Early Triassic sediments were therefore derived from North China (including the IMPU). In summary, zircon U–Pb and Hf isotopic data reveal that the sources of the Permian–Early Triassic sediments were the IMPU and North China craton, without any input from the juvenile materials from the southern CAOB north of the Bayan Obo–Chifeng fault.

Permian–Early Triassic retroarc foreland system in northern North China. The tectonic setting of the Permian–Early Triassic sedimentation in northern North China is critical for understanding the orogenic architecture of the southeast CAOB and the palaeogeography of northeast Pangaea. Sedimentological and provenance characteristics in this study support their deposition in a retroarc foreland basin. The Permian Dahongshan Formation in the Wuyuan area and the Permian–Early Triassic sediments in the Tumid area are thick, nonmarine siliciclastic successions. They unconformably overlie, or are in fault contact with, Palaeoproterozoic basement or early Palaeozoic passive margin littoral carbonate of the North China craton. The development of fold-and-thrust structures indicates a compressional tectonic environment for the Permian sedimentation (Supplementary Fig. 3b, c, g). The conglomerate of the Permian–Triassic sediments contains pebbles of granite, porphyrite, gneiss and quartzite (Supplementary Fig. 3f), and the sandstones contain variable amounts of quartz, feldspar and lithic fragments of granite, volcanic rocks, gneiss, schist and quartzite. The detrital zircon U–Pb age and Hf isotopic data further demonstrate that the IMPU and North China were the source regions. This dual provenance characterised by active magmatism juxtaposed with compressional deformation of the stable craton resulting in continental uplift is consistent with many well-studied retroarc foreland basins such as those developed in the Andes and throughout the Cordillera^{42,43}.

The IMPU has been demonstrated to be a late Palaeozoic Andean-type continental arc on the northern margin of North China that was initiated by the southward subduction of the PAO in the late Carboniferous^{31,32}. The main components of the continental arc are calc-alkaline or high-K calc-alkaline, metaluminous Permo–Carboniferous quartz diorite, diorite, granodiorite, tonalite, hornblende gabbro, I-type granites and adakites, with minor intermediate-acid volcanic lavas and tuffs³². The rock associations as well as geochemical and Sr–Nd–Hf isotopic data of the Permo–Carboniferous magmatism are consistent with an Andean-type continental arc^{32,44}. The build-up of the magmatic arc generated a topographic load on the northern margin of North China, the subsidence of which accommodated the deposition of the early Permian sediments.

Available data indicate that the Permian–Early Triassic retroarc foreland system might have developed along the entire northern margin of North China. A Permian retroarc foreland basin has recently been recognised in the Langshan area of the northern margin of the Alxa Block to the west of the study area (Fig. 1a). Thrust-imbricated pyroclastic materials eroded from the late Carboniferous–Permian continental arc and sediments eroded from the Precambrian basement of the Alxa Block were deposited in the retroarc foreland basin⁴⁵. Sedimentological and sandstone petrographic studies of the marginal marine to nonmarine alluvial Pyeongan Supergroup in Korea suggests that it was deposited in a retroarc foreland basin along the northern margin of North China between 320–250 Ma (ref. 46). These apparently isolated late Carboniferous to Early Triassic sedimentary successions might have once connected along-strike to form a continuous, >2000-km-long, east-west trending retroarc foreland system along the northern margin of North China ascribed to southward subduction of the PAO.

Permian Andean-type orogenic plateau in northern North China and its palaeoclimate implications.

Before deposition of the early Permian Dahongshan and Shuanmazhuang Formations, the northern margin of North China was covered by Cambrian–Ordovician shallow marine deposits dominated by quartz sandstone and carbonate rocks, representing a north-facing passive continental margin. Silurian to early Carboniferous sedimentation is generally lacking across the northern margin of North China due to limited weathering of the then low-relief cratonic margin. Subduction of the PAO beneath North China since late Carboniferous generated a continental magmatic arc, namely, the IMPU^{32,44}. The ~290 Ma Dahongshan and Shuanmazhuang Formations contain thick-bedded, coarse-grained conglomerates (Supplementary Fig. 2d, e) that were probably deposited in a proximal alluvial fan. This sedimentary change over time indicates that a progressive increase in relief of the nearby source areas was enough to generate debris flows during intense precipitation events in the early Permian. Detrital zircon U–Pb ages and Hf isotopic data indicate that the dominant sources for the early Permian sediments were derived from the IMPU. Therefore, the conglomerates of the Dahongshan and Shuanmazhuang Formations documented a phase of significant topographic growth and erosion of the IMPU by ~290 Ma. The uplift of the continental arc is also manifest in the abrupt increase in the proportions of late Palaeozoic detrital zircons in samples 21DHS07, 21DHS08 and 21DHS16 from the Dahongshan Formation (Supplementary Fig. 5c), which indicates accelerated erosion of the magmatic arc by ~290 Ma.

Our estimate of ~58 km for the average crustal thickness of northern North China during the latest Carboniferous–Permian is significantly greater than the average thickness of global continental crust (37 km), suggesting the existence of a high-

elevation orogenic plateau (Fig. 4). This crustal thickness is comparable to that of the Late Cretaceous to early Palaeogene central United States Cordillera (Nevadaplano, 55–65 km; ref. 47) and the southern United States–northern Mexico Cordillera (57 km; ref. 48), and is only slightly lower than the average crustal thickness (60–70 km) beneath the highest elevations in the Altiplano of the Central Andes⁴⁹. Assuming Airy isostatic compensation with an average crustal density of 2.77 g cm^{-3} , an average mantle density of 3.27 g cm^{-3} , and an average continental crust thickness of 37 km, our data indicate that the IMPU would have attained a palaeoelevation of $3.8 \pm 0.7 \text{ km}$ during the Permian. This palaeoelevation of the northern North China continental magmatic arc in northeast Pangaea is strikingly comparable to that of the late Carboniferous Variscan Belt ($3.4 \pm 0.7 \text{ km}$) of Western Europe within the core of Pangaea⁵⁰. Hornblende thermobarometry on late Carboniferous granitic plutons also indicates that large-scale uplift and exhumation of the IMPU occurred from the late Carboniferous to Early Jurassic and at least 15 km of crust was eroded during this period⁵¹. A more complete picture of palaeotopography during the assembly of Pangaea is thus emerging, with implications for palaeoclimatic conditions across the supercontinent.

The shift in sedimentary facies documented here from early Permian coal-bearing paralic and alluvial fan deposits to late Permian–Early Triassic continental redbeds reveals a dramatic climate change in North China (Fig. 2). The transition from a humid to an arid climate of North China during the Permian has also been documented by several other geological and palaeoclimate records. The identification of abundant plant macrofossil assemblages with diverse Cathaysian flora, along with massive coal deposits, in the Taiyuan and Shansi Formations in central Shaanxi Province, suggests that North China had a rather humid climate⁵². A clear palaeoclimate drying tendency from the late Artinskian–early Kungurian onwards is indicated by the increase in xerophytic plants and decrease in coal deposits in the upper Shansi Formation and Lower Shihhotse Formation in the Ordos Basin⁵³. In Shanxi Province, the Sunjiagou Formation, containing aeolian sandstone, gypsum and carbonate breccias with few plant fossils, rests unconformably on the Upper Shihhotse Formation palaeosols with abundant flora, which indicates a prominent shift from a subhumid environment to a more arid condition across the unconformity¹⁰. The gradual upward diminishing of black mudstone, along with the decrease of chemical index of alteration (CIA) values and total organic carbon (TOC) content over time, indicate long-term drying of North China from the early to middle Permian⁵⁴.

Previous studies simply attributed the Permian aridification of North China to continental drift through subtropical horse latitudes or temperature arid climate zone^{55,56}, without considering the possible impact of high topography created by accretionary/collisional orogenesis on the northern margin of North China. However, the sparse palaeomagnetic database for the Permian palaeolatitudes of North China suggests that it remained stable at $\sim 5^\circ \text{N}$ from the earliest Permian ($\sim 300 \text{ Ma}$) through late Permian ($\sim 260 \text{ Ma}$), and only eventually drifted northward into the $15\text{--}35^\circ \text{N}$ evaporite belt in the Triassic ($\sim 240 \text{ Ma}$; ref. 57). Therefore, available palaeomagnetic data do not support the idea that the northward drift of North China was responsible for the changes in sedimentary facies and climate described here as the tectonic transit critically post-dates the Permian climatic transition.

Alternatively, the Permian aridification was suggested to have resulted from an orographic rain shadow effect due to tectonic uplift associated with the collision between the Altaid arcs and North China¹⁵, although no detailed information on the scale and height of this topography was mentioned. This interpretation was

based on the premise that the arc-continent collision between the Altaids and North China was underway during the Permian. However, this assumption is not supported by regional geological and provenance data. Firstly, all the samples in this study, irrespective of their depositional ages, display similar detrital zircon U–Pb age populations and Hf isotopic compositions, indicating that they have similar provenance characteristics. This observation is inconsistent with a Permian collision between the Altaid arcs and North China, in which a prominent provenance change would have occurred in the foreland sediments in response to arc-continent collision. The lack of early Palaeozoic and Mesoproterozoic–Neoproterozoic detrital zircon U–Pb ages implies that the terranes north of the Bayan Obo–Chifeng fault contributed no detritus to the Permian–Early Triassic sediments, thus indicating that the southern CAOB was probably separated from North China by an ocean (the PAO) during Permian–Early Triassic (Fig. 5). Such an interpretation is consistent with the provenance of late Palaeozoic to Mesozoic strata from the Xishan area near Beijing that shows detritus from the juvenile crust of the Xing’an–Inner Mongolia orogenic belt had not reached North China until the Late Triassic⁵⁸. Secondly, the youngest blueschist facies metabasic rocks in Inner Mongolia have protolith ages of 239–235 Ma, indicating ongoing oceanic plate subduction until at least Middle Triassic⁵⁹. Further west, the youngest sandstone matrix of the Kanguer accretionary mélange in the East Tianshan containing tectonic blocks of normal mid-ocean ridge basalts (NMORB) has a maximum depositional age of $\sim 234 \text{ Ma}$ (ref. 60), indicating that the PAO was still being subducted in the Triassic. Detrital zircon provenance data from the Muzitekexie fore-arc accretionary basin, integrated with the compilation of regional multi-disciplinary evidence, suggest that oceanic subduction was ongoing until the Early Triassic in the South Tianshan⁶¹. The provenance analyses of Triassic retroarc sediments in the foreland of the Alxa Block suggests that the PAO was finally closed during Middle–Late Triassic (240–232 Ma; ref. 14). Thirdly, Permian sedimentation in the Nomgon and Bulgan Uul basins in southern Mongolia⁶² and in the Yin’e Basin in northern Alxa Block in China⁶³ is characterised by shallow marine turbidite fan deposition. Contrasting sedimentary facies existed on different sides of the Solonker suture zone until the latest Permian. Our provenance analysis in this study is consistent with regional geological data that suggest the PAO was continuously subducted beneath the northern margin of North China throughout the Permian–Early Triassic.

The Hercynian orogenesis resulted from the closure of the Rheic Ocean and subsequent collision between the Laurentia and Gondwanaland led to the assembly of the supercontinent Pangaea. Global climate studies based on sedimentary facies and palaeontological data indicate that the climate of Pangaea as a whole transitioned from icehouse to hothouse during the middle Permian⁵⁵. The formation of the supercontinent modified the source of moisture advection from the ocean to the continents and resulted in the development of large arid areas in the west and central Pangaea⁶⁴. The global aridification of Pangaea began in middle Pennsylvanian ($\sim 315 \text{ Ma}$) as represented by the change of terrestrial tropical wetland vegetation. The change did not encompass the entire Pangaea tropics, extending through Euramerica but not into China, where middle Pennsylvanian-type vegetation persisted well into the Permian in wetland environments⁶⁵. Therefore, the Permian aridification of North China occurred well after that of the western Pangaea¹⁰. Moreover, the provenance data in this study and most palaeogeographic reconstructions based on palaeomagnetic data support that the North China was separated from the main Pangaea by the Palaeo-Tethys Ocean and Palaeo-Asian Ocean during the Permian^{57,66}. The Permian aridification of North

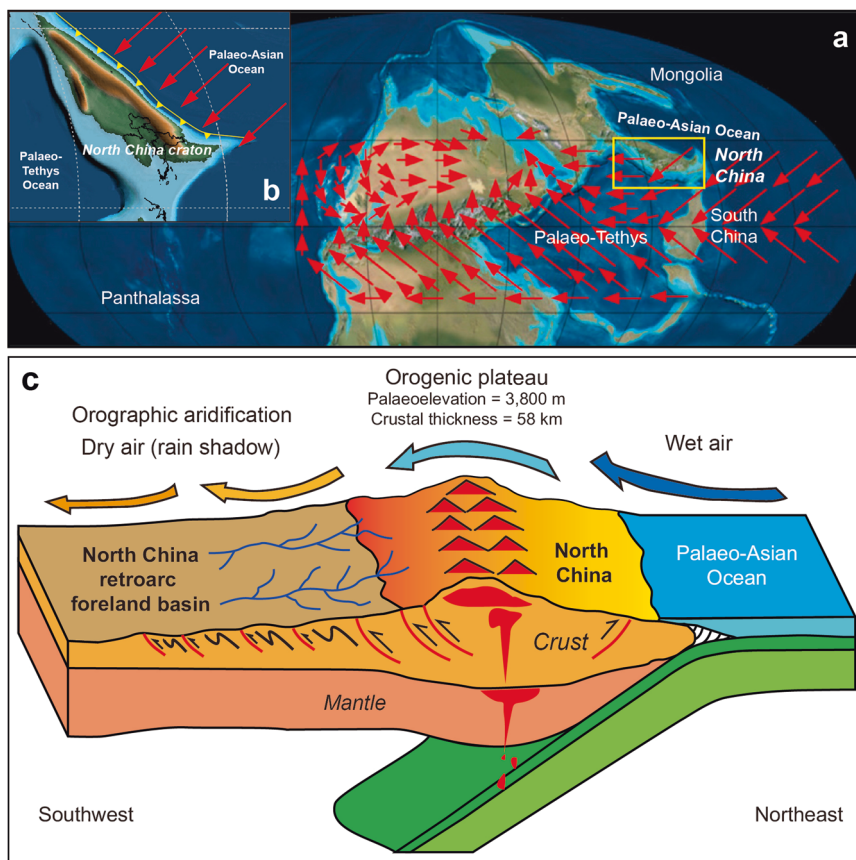


Fig. 5 Andean-like aridification model for Permian North China. **a** Global palaeogeographic reconstruction (~280 Ma) showing the tectonic position of North China, with modelled moisture transport directions indicated (adapted with permission from ref. ⁶⁴, Elsevier). **b** Close-up view showing the northwest-southeast trending mountain ranges (adapted with permission from ref. ⁷⁰, Annual Reviews) along the northern North China and the northeast wind. **c** The development of an Andean-type orogenic plateau with a palaeoelevation of ~3,800 m blocked the moisture transported from the Palaeo-Asian Ocean and played an important role in the Permian aridification of North China. Topography is vertically exaggerated.

China was therefore unlikely induced by the uplift of the Hercynian Mountains.

An increase in atmospheric CO₂ caused by Permian large igneous province (LIP) volcanism and associated Southern Hemisphere deglaciation has been considered the major driving force for the Permian drying in North China, presumably due to elevated surface temperature and evaporation that reduced soil moisture and the source of continental convective precipitation^{10,54}. The long term increase in atmospheric CO₂ may have led to long-term aridification in equatorial Pangaea as indicated by numeric climate model results⁶⁴. However, on shorter timescales, the stratigraphic record may not wholly support this relationship; for example, continental drying in western equatorial Pangaea predates the rise in atmospheric CO₂ (ref. ⁶⁷). The lithologic, stratigraphic and field relationship evidence in this study indicates that the Permian aridification in North China might have occurred after a major tectonic uplift event as represented by the deposition of the thick-bedded conglomerate in between the opposite palaeoclimatic conditions (Fig. 2). A similar situation was also reported in the Permian stratigraphy in Shanxi Province where increased aridity occurred after the formation of a major unconformity¹⁰. These geological records demonstrate that the Permian aridification cannot be interpreted alone by the increase of atmospheric CO₂. The role of topography growth during accretionary orogenesis must be taken into account when discussing the mechanism for the Permian aridification of North China.

Regional uplifts due to oceanic subduction and accretionary orogenesis along active continental margins, such as the Andes and elsewhere in the Cordillera, have been shown unequivocally to cause increasing aridity in the leeward slope^{68,69}. Our provenance analyses combined with previous studies indicate that the northern margin of North China was an Andean-type active continental margin that was initiated in the late Carboniferous and culminated in the Permian, ascribed to the southward subduction of the PAO. The ~58 km thickness of continental crust and ~3,800 m palaeoelevation estimated here for northern North China covered at least the area between ~40°59'N and ~42°48'N latitude and ~106°19'E and ~119°42'E longitude (present coordinates; Fig. 1b). Palaeogeographic reconstructions have showed that North China trended northwest-southeast during the Permian^{57,70,71}. The prevailing wind direction in North China was probably northeast⁶⁴ as it was located at the lower latitude of the Northern Hemisphere, which was nearly perpendicular to the orientation of the mountain ranges along the northern margin of North China. All the evidence suggests that the orogenic plateau would have been high and big enough to act as a physiographic barrier to prevent moisture transported from the north-northeast⁶⁴ reaching the foreland (Fig. 5). This would result in decreasing precipitation and increasing aridity in the leeward side. High-precision zircon U-Pb dating on tuffaceous rocks indicates that the aridification of North China was underway by the early Permian¹⁰. Based on our synthesis of available geological data, we propose that the Permian aridification of North China was dominantly the result

of an orographic rain shadow effect due to the uplift of the northern active continental margin of North China (Fig. 5), similar to the role of the Andes in forming the Atacama Desert as well as other arid regions of the Cordillera.

Methods

Zircon U-Pb and Hf isotopic analyses. Zircon grains were separated by crushing, heavy-liquid and magnetic methods, and then were randomly (regardless of their grain size, shape, colour and degree of rounding) mounted in epoxy resin and polished to expose the interior. Cathodoluminescence (CL) imaging was conducted with a scanning electron microscope at the Institute of Geology and Geophysics, Chinese Academy of Sciences, to select suitable grains and optimal target sites (avoiding cracks and inclusions) for U-Pb dating and Lu-Hf isotopic analyses.

Zircon U-Pb dating was conducted using LA-ICPMS in Nanjing Hongchuang Geological Exploration Technology Service Co., Ltd. The Resolution SE model laser ablation system (Applied Spectra, USA) was equipped with ATL (ATLEX 300) excimer laser and a Two Volume S155 ablation cell. The laser ablation system was coupled to an Agilent 7900 ICPMS (Agilent, USA). Detailed tuning parameters can be found in Thompson et al.⁷². Pre-ablation was conducted for each spot analysis using 5 laser shots (~0.3 µm in depth) to remove potential surface contamination. The analysis was performed using 30 µm diameter spot at 5 Hz and a fluence of 2 J cm⁻². Age calculations were conducted using IsoplotR (ref. 73). Zircon 91500 and GJ-1 was used as primary and secondary reference materials respectively. 91500 was analysed twice and GJ-1 analysed once every 10–12 analysis of the sample. Typically, 35–40 seconds of the sample signals were acquired after 20 seconds gas background measurement. NIST 610 and ⁹¹Zr were used to calibrate the trace element concentrations as external reference material and internal standard element respectively. During the seven batches of zircon U-Pb analysis, 151 spots on Zircon 91500 and 78 spots on Zircon GJ-1 were analysed respectively. The weighted mean ²⁰⁶Pb/²³⁸U ages of the Zircon 91500 reference materials for each batch are 1062.6 ± 3.4 Ma (*n* = 25, MSWD = 0.79), 1062.6 ± 2.5 Ma (*n* = 21, MSWD = 0.20), 1062.7 ± 2.7 Ma (*n* = 26, MSWD = 0.95), 1062.5 ± 3.5 Ma (*n* = 26, MSWD = 0.84), 1062.1 ± 2.6 Ma (*n* = 29, MSWD = 0.78), 1063.1 ± 5.5 Ma (*n* = 10, MSWD = 0.73) and 1062.5 ± 4.3 Ma (*n* = 13, MSWD = 0.19), respectively. The measured ages of the Zircon GJ-1 reference materials for each batch are 606.1 ± 2.6 Ma (*n* = 13, MSWD = 0.42), 608.8 ± 1.8 Ma (*n* = 11, MSWD = 1.2), 603.3 ± 2.0 Ma (*n* = 12, MSWD = 0.61), 605.7 ± 2.7 Ma (*n* = 13, MSWD = 0.45), 602.3 ± 1.9 Ma (*n* = 15, MSWD = 0.42), 604.0 ± 4.3 Ma (*n* = 5, MSWD = 1.3) and 606.2 ± 3.0 Ma (*n* = 8, MSWD = 0.82), respectively. These measured ages all agreed well with the reference value (1062.4 ± 0.4 Ma for 91500 and 600.7 ± 1.1 Ma for GJ-1, ref. 74) within uncertainty. A discordance filter of 20% was used for the U-Pb ages following ref. 75. The detrital zircon U-Pb ages are plotted as histograms and KDEs using DensityPlotter⁷⁶. In this study, ²⁰⁶Pb/²³⁸U ages are quoted for ages younger than 1000 Ma; otherwise, the ²⁰⁷Pb/²⁰⁶Pb ages are presented.

Hf isotope measurements were performed using a Thermo Finnigan Neptune-plus MC-ICP-MS fitted with a J-100 femto-second laser ablation system. Analyses of standard zircons 91500 and Plešovice over the measurement period provide weighted mean ¹⁷⁶Hf/¹⁷⁷Hf values of 0.282297 ± 0.000021 (2σ) and 0.282480 ± 0.000015 (2σ), respectively, consistent with the recommended ¹⁷⁶Hf/¹⁷⁷Hf values of 0.282307 ± 0.000031 (2σ; ref. 77) and 0.282482 ± 0.000013 (2σ; ref. 78), respectively. The isotopic ratio of ¹⁷⁶Hf/¹⁷⁷Hf was normalised to ¹⁷⁹Hf/¹⁷⁷Hf = 0.7325 (ref. 79) for mass bias correction. ¹⁸⁰Hf/¹⁷⁷Hf ratio was calculated to monitor the accuracy of the date and yielded an average value of

1.88688 (MSWD = 1.5, *n* = 266) for the analytical session (standards and unknowns), which is within the range of values reported by ref. 80. The decay constant for ¹⁷⁶Lu and the chondritic ratios of ¹⁷⁶Hf/¹⁷⁷Hf and ¹⁷⁶Lu/¹⁷⁷Hf used in calculations are 1.865 × 10⁻¹¹ year⁻¹ (ref. 81), and 0.282772 and 0.0332 (ref. 82), respectively. Initial ¹⁷⁶Hf/¹⁷⁷Hf ratios and ε_{Hf(t)} values are calculated by zircon crystallisation ages.

Crustal thickness estimation. Sr/Y and La/Yb are commonly used in igneous petrology to infer depths of magmatic diversification due to difference in the partition coefficient between these elements in various residual phases and intermediate melt^{83,84}. Profeta et al.⁸⁵ showed that whole-rock Sr/Y and La/Yb can be used as crustal thickness proxies in low magnesium intermediate calc-alkaline igneous rocks covering the compositional range of andesites and dacites and their intrusive equivalents. The empirical formula between whole-rock La/Yb and Moho depth for modern continental arcs⁸⁵ was applied to estimate the crustal thickness of northern North China. The lower degree of scatter in global and regional correlations for La/Yb makes it a more reliable indicator of thicker crust in continental arcs compared to that of Sr/Y⁸⁵. A compositional filter of SiO₂ = 55–70 wt%, MgO = 1–4 wt% and Rb/Sr = 0.05–0.25 (ref. 48,85) was applied in this study, in order to select suitable rock samples for crustal thickness estimation. This data filtering method ensures that only intermediate-composition rocks were used in the calculation, while mafic rocks generated in the mantle and high silica rocks formed by melting of middle-upper continental crust or from highly fractionated melts were eliminated⁸⁵. We compiled only unmineralized and minimally altered samples in this study. The filtered data set consisted of 57 whole-rock geochemical analyses that came from locations between 40°59'N and 42°48'N latitude and 106°19'E and 119°42'E longitude (present coordinates). The compiled samples ranged in crystallisation ages from 315 to 252 Ma (peak at ~280 Ma). Sample information, geochemical data and individual crustal thickness estimate are presented in Supplementary Data 4.

Bin size selection of histograms of occurrence data was guided by the crustal thickness data (*n* = 57; Fig. 4). According to Sturge's rule⁸⁶, the number of class intervals (bins), *K*, can be expressed as:

$$K = 1 + 3.322 \log_n \quad (1)$$

where *n* is the number of observations in the set. With 57 estimates of crustal thickness, then *K* = 6.8.

Data availability

Supplementary figures and the datasets that support the findings of this study, including the compilation of regional geochronological and geochemical data, are provided in Supplementary Information and Supplementary Data 1–4. All data are available in the online open access repository at <https://osf.io/wecvh/>.

Received: 8 July 2022; Accepted: 24 August 2023;

Published online: 04 September 2023

References

1. Strecker, M. R. et al. Tectonics and climate of the Southern Central Andes. *Annu. Rev. Earth Planet. Sci.* **35**, 747–787 (2013).
2. Li, Z.-X. et al. Magmatic switch-on and switch-off along the South China continental margin since the Permian: transition from an Andean-type to a Western Pacific-type plate boundary. *Tectonophysics* **532–535**, 271–290 (2012).
3. Montañez, I. P. & Poulsen, C. J. The late Paleozoic ice age: an evolving paradigm. *Annu. Rev. Earth Planet. Sci.* **41**, 629–656 (2013).

4. Poulsen, C. J., Pollard, D., Montañez, I. P. & Rowley, D. Late Paleozoic tropical climate response to Gondwanan deglaciation. *Geology* **35**, 771–774 (2007).
5. Goddérís, Y. et al. Onset and ending of the late Palaeozoic ice age triggered by tectonically paced rock weathering. *Nat. Geosci.* **10**, 382–386 (2017).
6. Şengör, A. M. C., Natal'in, B. A. & Burtman, V. S. Evolution of the Altaid tectonic collage and Palaeozoic crustal growth in Eurasia. *Nature* **364**, 299–307 (1993).
7. Xiao, W. et al. Accretionary processes and metallogensis of the Central Asian Orogenic Belt: Advances and perspectives. *Sci. China Earth Sci.* **63**, 329–361 (2020).
8. Song, S. et al. Ophiolites in the Xing'an-Inner Mongolia accretionary belt of the CAOB: implications for two cycles of seafloor spreading and accretionary orogenic events. *Tectonics* **34**, 2015TC003948 (2015).
9. Xiao, W., Windley, B. F., Hao, J. & Zhai, M. Accretion leading to collision and the Permian Solonker suture, Inner Mongolia, China: Termination of the central Asian orogenic belt. *Tectonics* **22**, 1069 (2003).
10. Wu, Q. et al. High-precision U–Pb age constraints on the Permian floral turnovers, paleoclimate change, and tectonics of the North China block. *Geology* **49**, 677–681 (2021).
11. Xiong, C. et al. Plant resilience and extinctions through the Permian to Middle Triassic on the North China Block: a multilevel diversity analysis of macrofossil records. *Earth-Sci. Rev.* **223**, 103846 (2021).
12. Xiao, W. et al. A Tale of amalgamation of three Permo-Triassic collage systems in Central Asia: oroclinal sutures, and terminal Accretion. *Ann. Rev. Earth Planet. Sci.* **43**, 477–507 (2015).
13. Cocks, L. R. M. & Torsvik, T. H. The dynamic evolution of the Palaeozoic geography of eastern Asia. *Earth-Sci. Rev.* **117**, 40–79 (2013).
14. Song, D. et al. Closure of the Paleo-Asian Ocean in the Middle-Late Triassic (Ladinian-Carnian): evidence from provenance analysis of retroarc sediments. *Geophys. Res. Lett.* **48**, e2021GL094276 (2021).
15. Cope, T., Ritts, B. D., Darby, B. J., Fildani, A. & Graham, S. A. Late Paleozoic sedimentation on the northern margin of the North China Block: implications for regional tectonics and climate change. *Int. Geol. Rev.* **47**, 270–296 (2005).
16. Chen, Y., Zhang, Z., Li, K., Yu, H. & Wu, T. Detrital zircon U–Pb ages and Hf isotopes of Permo-Carboniferous sandstones in central Inner Mongolia, China: implications for provenance and tectonic evolution of the southeastern Central Asian Orogenic Belt. *Tectonophysics* **671**, 183–201 (2016).
17. Flemings, P. B. & Jordan, T. E. A synthetic stratigraphic model of foreland basin development. *J. Geophys. Res. Solid Earth* **94**, 3851–3866 (1989).
18. BGMRNM (Bureau of Geology and Mineral Resources of Nei Mongol Autonomous Region. *Regional Geology of Nei Mongol Autonomous Region*. p. 725 (Geological Publishing House: Beijing, 1991).
19. Collinson J. D. *Sedimentary Environments: Processes, Facies, And Stratigraphy* (ed Reading H. G.) (Blackwell Science, 1996).
20. Allen, J. R. L. Studies in fluvialite sedimentation: a comparison of fining-upwards cyclothems, with special reference to coarse-member composition and interpretation. *J. Sediment. Res.* **40**, 298–323 (1970).
21. Zhang, S.-H., Zhao, Y., Ye, H., Liu, J.-M. & Hu, Z.-C. Origin and evolution of the Bainaimiao arc belt: Implications for crustal growth in the southern Central Asian orogenic belt. *Geol. Soc. Am. Bulletin*. **126**, 1275–1300 (2014).
22. Zhang, W., Jian, P., Kröner, A. & Shi, Y. Magmatic and metamorphic development of an early to mid-Paleozoic continental margin arc in the southernmost Central Asian Orogenic Belt, Inner Mongolia, China. *J. Asian Earth Sci.* **72**, 63–74 (2013).
23. Zhou, H., Zhao, G., Han, Y., Wang, B. & Pei, X. Tectonic origin of the Bainaimiao arc terrane in the southern Central Asian orogenic belt: Evidence from sedimentary and magmatic rocks in the Damao region. *GSA Bull.* **133**, 802–818 (2021).
24. Jian, P. et al. Evolution of a Permian intraoceanic arc-trench system in the Solonker suture zone, Central Asian Orogenic Belt, China and Mongolia. *Lithos* **118**, 169–190 (2010).
25. Li, J., Guo, F., Li, C., Zhao, L. & Huang, M. Permian back-arc extension in central Inner Mongolia, NE China: Elemental and Sr–Nd–Pb–Hf–O isotopic constraints from the Linxi high-MgO diabase dikes. *Island Arc* **24**, 404–424 (2015).
26. Jian, P. et al. Time scale of an early to mid-Paleozoic orogenic cycle of the long-lived Central Asian Orogenic Belt, Inner Mongolia of China: Implications for continental growth. *Lithos* **101**, 233–259 (2008).
27. Li, Y., Brouwer, F. M., Xiao, W. & Zheng, J. Late Devonian to early Carboniferous arc-related magmatism in the Baolidao arc, Inner Mongolia, China: significance for southward accretion of the eastern Central Asian orogenic belt. *Geol. Soc. Am. Bull.* **129**, 677–697 (2017).
28. Tong, Y. et al. Permian alkaline granites in the Erenhot–Hegenshan belt, northern Inner Mongolia, China: Model of generation, time of emplacement and regional tectonic significance. *J. Asian Earth Sci.* **97**, 320–336 (2015).
29. Li, Y. et al. Subduction initiation in the southeastern Palaeo-Asian Ocean: Constraints from early Permian adakites in suprasubduction zone ophiolites, central Inner Mongolia, North China. *Geol. J.* **55**, 2044–2061 (2020).
30. Zhang, X., Yuan, L., Xue, F., Yan, X. & Mao, Q. Early Permian A-type granites from central Inner Mongolia, North China: magmatic tracer of post-collisional tectonics and oceanic crustal recycling. *Gondwana Res.* **28**, 311–327 (2015).
31. Zhang, S.-H. et al. Contrasting Late Carboniferous and Late Permian–Middle Triassic intrusive suites from the northern margin of the North China craton: Geochronology, petrogenesis, and tectonic implications. *Geol. Soc. Am. Bull.* **121**, 181–200 (2009).
32. Zhang, S.-H. et al. Early Permian plutons from the northern North China Block: constraints on continental arc evolution and convergent margin magmatism related to the Central Asian Orogenic Belt. *Int. J. Earth Sci.* **98**, 1441–1467 (2009).
33. Zhang, S.-H. et al. Late Paleozoic to Early Mesozoic mafic–ultramafic complexes from the northern North China Block: Constraints on the composition and evolution of the lithospheric mantle. *Lithos* **110**, 229–246 (2009).
34. Zhang, X. et al. Mafic and felsic magma interaction during the construction of high-K calc-alkaline plutons within a metacratonic passive margin: The Early Permian Guyang batholith from the northern North China Craton. *Lithos* **125**, 569–591 (2011).
35. Luo, H. L., Wu, T. R. & Li, Y. Geochemistry and SHRIMP dating of the Kebu massif from Wulatezhongqi, Inner Mongolia: evidence for the early Permian underplating beneath the North China Craton. *Acta Petrol. Sin.* **23**, 755–766 (2007).
36. Zhang, X., Zhang, H., Jiang, N., Zhai, M. & Zhang, Y. Early Devonian alkaline intrusive complex from the northern North China craton: a petrological monitor of post-collisional tectonics. *J. Geol. Soc.* **167**, 717–730 (2010).
37. Shi, Y. et al. Devonian A-type granitic magmatism on the northern margin of the North China Craton: SHRIMP U–Pb zircon dating and Hf-isotopes of the Hongshan granite at Chifeng, Inner Mongolia, China. *Gondwana Res.* **17**, 632–641 (2010).
38. Rojas-Agramonte, Y. et al. Detrital and xenocrystic zircon ages from Neoproterozoic to Palaeozoic arc terranes of Mongolia: Significance for the origin of crustal fragments in the Central Asian Orogenic Belt. *Gondwana Res.* **19**, 751–763 (2011).
39. Jian, P. et al. Episodic mantle melting-crustal reworking in the late Neoproterozoic of the northwestern North China Craton: Zircon ages of magmatic and metamorphic rocks from the Yinshan Block. *Precambrian Res.* **222**, 230–254 (2012).
40. Jian, P., Zhang, Q., Liu, D. Y. & Jin, W. SHRIMP dating and geological significance of Late Achaean high-Mg diorite (sanukite) and hornblende-granite at Guyang of Inner Mongolia. *Acta Petrol. Sin.* **21**, 151–157 (2005).
41. Song, D. et al. New chronological constraints on the tectonic affinity of the Alxa Block, NW China. *Precambrian Res.* **299**, 230–243 (2017).
42. Nie, J. et al. Integrated provenance analysis of a convergent retroarc foreland system: U–Pb ages, heavy minerals, Nd isotopes, and sandstone compositions of the Middle Magdalena Valley basin, northern Andes, Colombia. *Earth-Sci. Rev.* **110**, 111–126 (2012).
43. Laskowski, A. K., Decelles, P. G. & Gehrels, G. E. Detrital zircon geochronology of Cordilleran retroarc foreland basin strata, western North America. *Tectonics* **32**, 1027–1048 (2013).
44. Zhang, S. H. et al. Carboniferous granitic plutons from the northern margin of the North China block: implications for a late Paleozoic active continental margin. *J. Geol. Soc.* **164**, 451–463 (2007).
45. Tian, R. et al. Late Paleozoic Tectonic Evolution of the Paleo-Asian Ocean in the Northern Alxa Block (NW China). *Tectonics* **39**, e2020TC006359 (2020).
46. Choi, D. K. Evolution of the Taebaeksan Basin, Korea: II, late Paleozoic sedimentation in a retroarc foreland basin and assembly of the proto-Korean Peninsula. *Island Arc* **28**, e12277 (2019).
47. Chapman, J. B., Ducea, M. N., DeCelles, P. G. & Profeta, L. Tracking changes in crustal thickness during orogenic evolution with Sr/Y: an example from the North American Cordillera. *Geology* **43**, 919–922 (2015).
48. Chapman, J. B., Greig, R. & Haxel, G. B. Geochemical evidence for an orogenic plateau in the southern U.S. and northern Mexican Cordillera during the Laramide orogeny. *Geology* **48**, 164–168 (2019).
49. Ryan, J. et al. Central Andean crustal structure from receiver function analysis. *Tectonophysics* **682**, 120–133 (2016).
50. Dusséaux, C., Gébelin, A., Ruffet, G. & Mulch, A. Late Carboniferous paleoelevation of the Variscan Belt of Western Europe. *Earth Planet. Sci. Lett.* **569**, 117064 (2021).
51. Zhang, S. H., Zhao, Y. & Song, B. Hornblende thermobarometry of the Carboniferous granitoids from the Inner Mongolia Paleo-uplift: implications for the tectonic evolution of the northern margin of North China block. *Mineral. Petrol.* **87**, 123–141 (2006).
52. Wang, J. Late Paleozoic macrofloral assemblages from Weibei Coalfield, with reference to vegetational change through the late Paleozoic ice-age in the North China Block. *Int. J. Coal Geol.* **83**, 292–317 (2010).
53. Liu, F., Zhu, H. & Ouyang, S. Late Pennsylvanian to Wuchiapingian palynostratigraphy of the Baode section in the Ordos Basin, North China. *J. Asian Earth Sci.* **111**, 528–552 (2015).

54. Wang, Y. et al. Early–middle Permian drying in the North China Block induced by large igneous provinces. *Palaeogeogr. Palaeoclimatol. Palaeoecol.* **592**, 110922 (2022).
55. Rees, P. M., Gibbs, M. T., Ziegler, A. M., Kutzbach, J. E. & Behling, P. J. Permian climates: evaluating model predictions using global paleobotanical data. *Geology* **27**, 891–894 (1999).
56. Ziegler, M. *Late glacial and postglacial environmental changes; Quaternary, Carboniferous–Permian, and Proterozoic.* (ed. Martini, I. P.) p. 111–142 (Oxford University Press, 1997).
57. Huang, B. et al. Paleomagnetic constraints on the paleogeography of the East Asian blocks during Late Paleozoic and Early Mesozoic times. *Earth-Sci. Rev.* **186**, 8–36 (2018).
58. Yang, J.-H. et al. Constraints on the timing of uplift of the Yanshan Fold and Thrust Belt, North China. *Earth Planet. Sci. Lett.* **246**, 336–352 (2006).
59. Zhang, J., Wei, C. & Chu, H. Blueschist metamorphism and its tectonic implication of late Paleozoic–early Mesozoic metabasites in the mélange zones, central Inner Mongolia, China. *J. Asian Earth Sci.* **97**, 352–364 (2015).
60. Ao, S. et al. The youngest matrix of 234 Ma of the Kanguer accretionary mélange containing blocks of N-MORB basalts: constraints on the northward subduction of the Paleo-Asian Kanguer Ocean in the Eastern Tianshan of the Southern Altai. *Int. J. Earth Sci.* **110**, 791–808 (2021).
61. Tan, Z. et al. Final closure of the Paleo Asian Ocean basin in the early Triassic. *Commun. Earth Environ.* **3**, 259 (2022).
62. Heumann, M. J. et al. Paleogeographic reconstruction of a late Paleozoic arc collision zone, southern Mongolia. *Geol. Soc. Am. Bull.* **124**, 1514–1534 (2012).
63. Song, D., Xiao, W., Windley, B. F. & Han, C. Provenance and tectonic setting of late Paleozoic sedimentary rocks from the Alxa Tectonic Belt (NW China): implications for accretionary tectonics of the southern Central Asian Orogenic Belt. *GSA Bull.* **133**, 253–276 (2021).
64. Tabor, N. J. & Poulsen, C. J. Palaeoclimate across the Late Pennsylvanian–Early Permian tropical palaeolatitudes: a review of climate indicators, their distribution, and relation to palaeophysiological climate factors. *Palaeogeogr. Palaeoclimatol. Palaeoecol.* **268**, 293–310 (2008).
65. Hilton, J. & Cleal, C. J. The relationship between Euramerican and Cathaysian tropical floras in the late Palaeozoic: palaeobiogeographical and palaeogeographical implications. *Earth-Sci. Rev.* **85**, 85–116 (2007).
66. Ren, Q. et al. New Early Permian paleomagnetic and geochronological data from the Xilinhot–Songliao Block and their implications for the relationship between the Paleo-Asian Ocean and the Paleo-Tethys Ocean. *Geophys. Res. Lett.* **49**, e2022GL100462 (2022).
67. Montañez, I. P. et al. CO₂-forced climate and vegetation instability during late Paleozoic deglaciation. *Science* **315**, 87–91 (2007).
68. Houston, J. & Hartley, A. J. The central Andean west-slope rainshadow and its potential contribution to the origin of hyper-aridity in the Atacama Desert. *Int. J. Climatol.: A J. R. Meteorol. Soc.* **23**, 1453–1464 (2003).
69. Allen, P. A., Verlander, J. E., Burgess, P. M. & Audet, D. M. Jurassic giant erg deposits, flexure of the United States continental interior, and timing of the onset of Cordilleran shortening. *Geology* **28**, 159–162 (2000).
70. Scotese, C. R. An atlas of Phanerozoic paleogeographic maps: the seas come in and the seas go out. *Annu. Rev. Earth Planet. Sci.* **49**, 679–728 (2021).
71. Zhang, D. et al. Quantifying the extent of the Paleo-Asian Ocean during the late Carboniferous to early Permian. *Geophys. Res. Lett.* **48**, e2021GL094498 (2021).
72. Thompson, J. M., Meffre, S. & Danyushevsky, L. Impact of air, laser pulse width and fluence on U–Pb dating of zircons by LA-ICPMS. *J. Anal. At. Spectrom.* **33**, 221–230 (2018).
73. Vermeesch, P. IsoplotR: A free and open toolbox for geochronology. *Geosci. Front.* **9**, 1479–1493 (2018).
74. Jackson, S. E., Pearson, N. J., Griffin, W. L. & Belousova, E. A. The application of laser ablation-inductively coupled plasma-mass spectrometry to in situ U–Pb zircon geochronology. *Chem. Geol.* **211**, 47–69 (2004).
75. Gehrels, G. *Tectonics of Sedimentary Basins: Recent advances* (eds C. Busby & A. Azor) (Wiley Blackwell, 2012).
76. Vermeesch, P. On the visualisation of detrital age distributions. *Chem. Geol.* **312–313**, 190–194 (2012).
77. Wu, F.-Y., Yang, Y.-H., Xie, L.-W., Yang, J.-H. & Xu, P. Hf isotopic compositions of the standard zircons and baddeleyites used in U–Pb geochronology. *Chem. Geol.* **234**, 105–126 (2006).
78. Sláma, J. et al. Plešovice zircon — a new natural reference material for U–Pb and Hf isotopic microanalysis. *Chem. Geol.* **249**, 1–35 (2008).
79. Patchett, P. J. & Tatsumoto, M. Hafnium isotope variations in oceanic basalts. *Geophys. Res. Lett.* **7**, 1077–1080 (1980).
80. Thirlwall, M. F. & Anczkiewicz, R. Multidynamic isotope ratio analysis using MC–ICP–MS and the causes of secular drift in Hf, Nd and Pb isotope ratios. *Int. J. Mass Spectrom.* **235**, 59–81 (2004).
81. Scherer, E., Münker, C. & Mezger, K. Calibration of the Lutetium–Hafnium Clock. *Science* **293**, 683–687 (2001).
82. Blichert-Toft, J. & Albarède, F. The Lu–Hf isotope geochemistry of chondrites and the evolution of the mantle–crust system. *Earth Planet. Sci. Lett.* **148**, 243–258 (1997).
83. Mantle, G. W. & Collins, W. J. Quantifying crustal thickness variations in evolving orogens: correlation between arc basalt composition and Moho depth. *Geology* **36**, 87–90 (2008).
84. Lee, C.-T. A., Morton, D. M., Kistler, R. W. & Baird, A. K. Petrology and tectonics of Phanerozoic continent formation: from island arcs to accretion and continental arc magmatism. *Earth Planet. Sci. Lett.* **263**, 370–387 (2007).
85. Profeta, L. et al. Quantifying crustal thickness over time in magmatic arcs. *Sci. Rep.* **5**, 17786 (2015).
86. Sturges, H. The choice of a class-interval. *J. Am. Stat. Assoc.* **21**, 65–66 (1926).
87. Windley, B. F. & Xiao, W. Ridge subduction and slab windows in the Central Asian Orogenic Belt: Tectonic implications for the evolution of an accretionary orogen. *Gondwana Res.* **61**, 73–87 (2018).

Acknowledgements

We are grateful to editors Joe Aslin and Maria Laura Balestrieri, as well as four anonymous reviewers, for their constructive comments and suggestions that substantially improved the quality of this paper. We declare that none of the sampling permissions were required. This work was financially supported by the National Natural Science Foundation of China (41888101 and 42222210), the Strategic Priority Research Program (B) of the Chinese Academy of Sciences (XDB26020301) and the Youth Innovation Promotion Association CAS (2021062). This is a contribution to IGCP 662.

Author contributions

D.S. and W.X. designed the project, initiated the idea, and designed the experiments; D.S., Q.M., B.W. and S.A. performed the experiments and analysed the data; D.S., R.N.M. and W.X. wrote the manuscript with inputs from all authors.

Competing interests

The authors declare no competing interests.

Additional information

Supplementary information The online version contains supplementary material available at <https://doi.org/10.1038/s43247-023-00976-2>.

Correspondence and requests for materials should be addressed to Dongfang Song, Ross N. Mitchell, Wenjiao Xiao or Songjian Ao.

Peer review information *Communications Earth & Environment* thanks Jifí Sláma, and the other, anonymous, reviewer(s) for their contribution to the peer review of this work. Primary Handling Editors: Maria Laura Balestrieri, Joe Aslin and Clare Davis. A peer review file is available.

Reprints and permission information is available at <http://www.nature.com/reprints>

Publisher's note Springer Nature remains neutral with regard to jurisdictional claims in published maps and institutional affiliations.



Open Access This article is licensed under a Creative Commons

Attribution 4.0 International License, which permits use, sharing, adaptation, distribution and reproduction in any medium or format, as long as you give appropriate credit to the original author(s) and the source, provide a link to the Creative Commons license, and indicate if changes were made. The images or other third party material in this article are included in the article's Creative Commons license, unless indicated otherwise in a credit line to the material. If material is not included in the article's Creative Commons license and your intended use is not permitted by statutory regulation or exceeds the permitted use, you will need to obtain permission directly from the copyright holder. To view a copy of this license, visit <http://creativecommons.org/licenses/by/4.0/>.

© The Author(s) 2023